Coastally Generated Near-Inertial Waves

SAMUEL M. KELLY

Large Lakes Observatory, and Physics and Astronomy Department, University of Minnesota Duluth, Duluth, Minnesota

(Manuscript received 20 July 2018, in final form 9 August 2019)

ABSTRACT

Wind directly forces inertial oscillations in the mixed layer. Where these currents hit the coast, the no-normal-flow boundary condition leads to vertical velocities that pump both the base of the mixed layer and the free surface, producing offshore-propagating near-inertial internal and surface waves, respectively. The internal waves directly transport wind work downward into the ocean's stratified interior, where it may provide mechanical mixing. The surface waves propagate offshore where they can scatter over rough topography in a process analogous to internal-tide generation. Here, we estimate mixed layer currents from observed winds using a damped slab model. Then, we estimate the pressure, velocity, and energy flux associated with coastally generated near-inertial waves at a vertical coastline. These results are extended to coasts with arbitrary across-shore topography and examined using numerical simulations. At the New Jersey shelfbreak, comparisons between the slab model, numerical simulations, and moored observations are ambiguous. Extrapolation of the theoretical results suggests that $\mathcal{O}(10\%)$ of global wind work (i.e., 0.03 of 0.31 TW) is transferred to coastally generated barotropic near-inertial waves.

1. Introduction

Wind work supplies 0.3–1.5 TW to near-inertial motion to the surface boundary layer (Alford et al. 2016). Where these currents converge and diverge they pump the sea surface and base of the mixed layer generating near-inertial waves. Near-inertial waves are ubiquitous in the deep ocean (e.g., Alford and Whitmont 2007), on the continental shelf (e.g., Shearman 2005), and in the Laurentian Great Lakes (e.g., Choi et al. 2012; Austin 2013). Several mechanisms produce near-inertial mixed layer pumping, including propagating storms (e.g., Price 1983; Gill 1984), latitudinal variation in the inertial frequency (i.e., the β effect; D'Asaro 1989; D'Asaro et al. 1995; Moehlis and Llewellyn Smith 2001), interactions with mesoscale features (e.g., Weller 1982; Young and Ben Jelloul 1997), and coastlines (e.g., Pettigrew 1980; Millot and Crépon 1981; Kundu et al. 1983). The relative importance of each process is unknown, although understanding them is critical for predicting near-inertial currents and estimating wind-driven mixing (e.g., Alford et al. 2016).

Here we investigate the generation of near-inertial waves at a coast (Fig. 1). Coastal near-inertial waves (CNIWs) arise as the transient response to shifting wind at a coast. The simplest models involve small-amplitude motions in two-layer or continuous stratification that are forced by a sudden wind over a flat ocean bounded on one side by straight coastline (Pettigrew 1980; Millot and Crépon 1981; Csanady 1982; Kundu et al. 1983; Kundu 1984; Baines 1986). A linear damping term is typically added to prevent singular resonance at the inertial frequency (Millot and Crépon 1981; Kundu et al. 1983). The resulting motion is simultaneously narrowband (i.e., peaked near the inertial frequency) and transient, so both time-domain and frequency-domain analyses are useful. Solutions in the time domain are readily obtained by Laplace transform (Pettigrew 1980; Millot and Crépon 1981; Csanady 1982; Kundu et al. 1983; Kundu 1984). In general, the solutions have (i) an offshore component associated with directly forced mixed layer currents, (ii) a coastal-trapped component associated with slowly evolving upwelling or downwelling, and (iii) a transient component associated with offshore radiating near-inertial waves. Despite many simplifying assumptions, these theoretical solutions compare well with observations (Pettigrew 1980; Millot and Crépon 1981; Shearman 2005).

Existing theories identify a mechanism for CNIW generation, however they do not (i) provide estimates of CNIWs in the presence of continuous observed winds, (ii) address the effects of variable cross-shore coastal

Corresponding author: Samuel M. Kelly, smkelly@d.umn.edu

DOI: 10.1175/JPO-D-18-0148.1

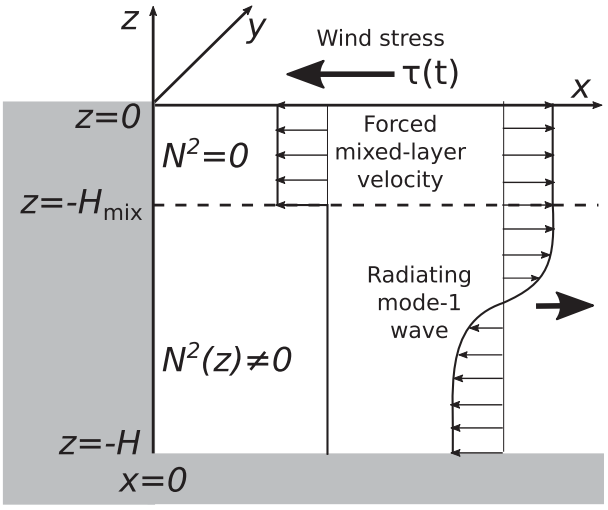

FIG. 1. Wind stress forces mixed layer currents that lift the sea surface or depress the base of the mixed layer when they impinge on the coast. Oscillating (i.e., near-inertial) mixed layer currents then generate offshore propagating surface and internal waves.

bathymetry, or (iii) assess the global relevance of CNIW generation as an energy pathway from the surface mixed layer to the stratified interior. Here, we reformulate Kundu et al.'s (1983) theory by separating forced and wave components (section 2) and derive the forced (section 3) and wave (section 4) solutions for continuous observed winds. Next, we use numerical simulations to examine the role of variable cross-shelf bathymetry (section 5). The paper concludes by estimating the global relevance of CNIW generation (section 6) and summarizing the results (section 7).

For simplicity, this paper retains Kundu et al.'s (1983) assumptions of uniform wind stress and inertial frequency, straight coastlines, and small-amplitude motions. Relaxing the first three assumptions would lead to open-water near-inertial wave generation (Gill 1984; D'Asaro 1989; D'Asaro et al. 1995; Moehlis and Llewellyn Smith 2001) and coastal-trapped waves (e.g., Brink 1991). Relaxing the small-amplitude assumption would allow nonlinear interactions between the wave and upwelling components of the solutions (Federiuk and Allen 1996; Chant 2001).

2. Equations of motion

The linearized, Boussinesq, hydrostatic momentum, continuity, and buoyancy equations,

$$\frac{\partial \mathbf{u}}{\partial t} + f\hat{\mathbf{k}} \times \mathbf{u} = -\nabla p + \frac{\partial \boldsymbol{\tau}}{\partial z}, \tag{1a}$$

$$0 = -\frac{\partial p}{\partial z} + b, \tag{1b}$$

$$\nabla \cdot \mathbf{u} + \frac{\partial w}{\partial z} = 0, \quad \text{and} \tag{1c}$$

$$\frac{\partial b}{\partial t} + wN^2 = 0, \tag{1d}$$

respectively, describe small-amplitude motions. Here, $\mathbf{u} = u\hat{\mathbf{i}} + v\hat{\mathbf{j}}$ and w are horizontal and vertical velocity, and f and $N(z)$ are the inertial and buoyancy frequencies. The buoyancy force $b = -g\rho/\rho_0$, pressure p, and viscous stress τ are normalized by a reference density ρ_0. The term ρ is the density perturbation and g is gravity. The boundary conditions are a flat bottom at $z = -H$, and a linear free surface at $z = 0$. The surface mixed layer ($N^2 = 0$) extends to $z = -H_{\text{mix}}$ (Fig. 1).

a. Separating forced and wave motion

We define the "forced response" as the velocity that balances the stress divergence in the absence of a pressure gradient:

$$\frac{\partial \overline{\mathbf{u}}}{\partial t} + f\hat{\mathbf{k}} \times \overline{\mathbf{u}} = \frac{\partial \boldsymbol{\tau}}{\partial z}. \tag{2a}$$

Subtracting the forced velocity from the full equations of motion yields the "wave response,"

$$\frac{\partial \mathbf{u}'}{\partial t} + f\hat{\mathbf{k}} \times \mathbf{u}' = -\nabla p', \tag{3a}$$

$$\frac{\partial}{\partial t}\left[\frac{\partial}{\partial z}\left(\frac{-1}{N^2}\frac{\partial p}{\partial z}\right)\right] + \nabla \cdot \mathbf{u}' = -\nabla \cdot \overline{\mathbf{u}}, \tag{3b}$$

where w and b have been eliminated, the primes denote wave velocities, and pressure is entirely associated with the wave response (i.e., $p = p'$). Divergences in forced velocities produce waves through the term on the right-hand side of (3b). In general, these divergences could be driven by horizontal variability in wind, stratification, or inertial frequency. Boundary conditions also produce waves by requiring no normal velocity at the coast (i.e., $u_\perp = 0$, which is equivalent to $u'_\perp = -\overline{u}_\perp$).

b. Projection onto vertical modes

Over a flat bottom, velocity and pressure are sums of uncoupled vertical modes,

$$\mathbf{u}(x, y, z, t) = \sum_{n=0}^{\infty} \mathbf{u}_n(x, y, t)\phi_n(z), \tag{4a}$$

$$p(x, y, z, t) = \sum_{n=0}^{\infty} p_n(x, y, t)\phi_n(z), \tag{4b}$$

where the modes ϕ_n and eigenspeeds c_n are determined by an eigenvalue problem with linear free-surface and flat-bottom boundary conditions (e.g., Wunsch 2015)

$$\frac{d}{dz}\left(\frac{1}{N^2}\frac{d\phi_n}{dz}\right)+\frac{1}{c_n^2}\phi_n=0, \tag{5a}$$

$$\frac{d\phi_n}{dz}=-\frac{N^2}{g}\phi_n \quad \text{at} \quad z=0, \quad \text{and} \tag{5b}$$

$$\frac{d\phi_n}{dz}=0 \quad \text{at} \quad z=-H, \tag{5c}$$

and the orthogonality/normalization condition

$$\frac{1}{H}\int_{-H}^{0}\phi_m\phi_n\,dz=\delta_{mn}. \tag{6}$$

Our sign convention is $\phi_n>0$ at $z=0$. Note that ϕ_n is constant in the mixed layer, where $N^2=0$.

To proceed, we must parameterize the vertical profile of stress divergence. For simplicity, we assume uniform stress divergence in the mixed layer and zero divergence below (i.e., there is no bottom drag). Integrating (2a) over the mixed layer produces

$$\frac{\partial\overline{\mathbf{U}}}{\partial t}+f\hat{\mathbf{k}}\times\overline{\mathbf{U}}=\boldsymbol{\tau}|_0-\boldsymbol{\tau}|_{-H_{\text{mix}}}, \tag{7}$$

where $\overline{\mathbf{U}}=H_{\text{mix}}\overline{\mathbf{u}}$ is mixed layer transport. We parameterize interfacial stress as $\boldsymbol{\tau}|_{-H_{\text{mix}}}=-r\overline{\mathbf{U}}$, where r is a damping parameter with empirical values of $r^{-1}=2$–5 days (Plueddemann and Farrar 2006). Wind stress is $\boldsymbol{\tau}|_0$, hereafter written as simply $\boldsymbol{\tau}$.

Incorporating the stress parameterization and projecting the wave response onto vertical modes yields

$$\left(\frac{\partial}{\partial t}+r\right)\overline{\mathbf{U}}+f\hat{\mathbf{k}}\times\overline{\mathbf{U}}=\boldsymbol{\tau}, \tag{8a}$$

$$\frac{\partial\mathbf{u}_n'}{\partial t}+f\hat{\mathbf{k}}\times\mathbf{u}_n'=-\nabla p_n', \quad \text{and} \tag{8b}$$

$$\frac{\partial p_n'}{\partial t}+c_n^2\nabla\cdot\mathbf{u}_n'=-c_n^2\overline{w}_n, \tag{8c}$$

where $\overline{w}_n=\nabla\cdot\overline{\mathbf{U}}\phi_n|_0/H$ forces the waves. Note, that $\overline{w}_n$ has units of per second, consistent with the convention of Kelly (2016).

c. Relation to other formulations

The preceding decomposition is more complicated than simply projecting wind stress onto each vertical mode (see, e.g., Pollard and Millard 1970; Kundu et al. 1983; Gill 1984), but the decomposition has two benefits. First, the damping parameterization is more flexible, allowing forced motions and low-mode internal waves to be dissipated at different rates. In fact, the formulation here only deviates from Kundu et al. (1983) in that damping is selectively applied to forced motion as opposed to all motion. As a result, mixed layer energy is bounded by viscous effects, while internal-wave energy is only bounded by inviscid offshore radiation.

The second benefit of the decomposition is that the resulting equations are familiar. The equation describing forced motion (8a) is the slab model introduced by Pollard (1970), which is mathematically equivalent to a simple harmonic oscillator. Slab models compare well with observed mixed layer currents (e.g., Plueddemann and Farrar 2006) and are convenient for estimating wind work (e.g., D'Asaro 1985; Alford 2001, 2003; Watanabe and Hibiya 2002; Jiang et al. 2005). The equations describing wave motion [(8b) and (8c)] are identical to the those derived by Llewellyn Smith and Young (2002) and Kelly et al. (2016) to describe topographic internal-tide generation, except that tidal forcing is $\overline{w}_n=\mathbf{u}_0\cdot\nabla H\phi_n|_{-H}$, where $\mathbf{u}_0$ is the surface tide. Thus, a wide range of analytical and numerical tools are immediately available to solve the equations.

The decomposition presented here has a notable drawback: the slab model is not a complete mixed layer model because directly integrating the full momentum equations over the mixed layer would add an additional term representing internal-wave drag (i.e., the term $-H_{\text{mix}}\nabla p'|_0$). In general, mixed layer currents are damped by both turbulence and internal-wave radiation. The latter effect likely dominates in the open ocean (e.g., Moehlis and Llewellyn Smith 2001), but is nonexistent in the idealized setting considered here, where there is no internal-wave generation except at the coast. Thus, tuning r to achieve reasonable forced velocities is effectively parameterizing both unresolved turbulence and offshore internal-wave radiation from the mixed layer. In some sense, the procedure is analogous to parameterizing wave drag in a surface-tide model (e.g., Jayne and St. Laurent 2001) and then using the resulting surface-tide velocities to force an internal-tide model.

d. Energy balances

The energy equation for forced motion, obtained by multiplying (8a) by $\overline{\mathbf{U}}/H_{\text{mix}}$, is

$$\frac{\partial}{\partial t}\left(\frac{1}{2}\frac{|\overline{\mathbf{U}}|^2}{H_{\text{mix}}}\right)=\frac{\boldsymbol{\tau}\cdot\overline{\mathbf{U}}}{H_{\text{mix}}}-\frac{r|\overline{\mathbf{U}}|^2}{H_{\text{mix}}}, \tag{9}$$

where the left-hand side is the rate of change in kinetic energy and the right-hand side is the rate of wind work minus the rate of energy dissipation.

The energy equation for the wave response, obtained by multiplying (8b) by $H\mathbf{u}_n'$, (8c) by Hp_n' and summing is

$$\frac{\partial}{\partial t}\left(\frac{H}{2}|\mathbf{u}_n'|^2+\frac{H}{2}\frac{p_n'^2}{c_n^2}\right)+\nabla\cdot(H\mathbf{u}_n'p_n')=C_w, \tag{10}$$

where the first term on the left-hand side is the rate of change of kinetic and potential energy, and the second term is energy flux divergence (energy flux in each mode is $F_n = H\mathbf{u}_n'p_n'$). The term on the right hand side is wind-driven wave generation $C_w = -H\overline{w}_n p_n'$ or, equivalently, $C_w = -\nabla\cdot\overline{\mathbf{U}}p_n'\phi_n|_0$.

For perfectly periodic motions, averaging these equations over a wave period reduces them to a steady-state balance between energy sources and sinks (e.g., wind work equals viscous dissipation, or wave generation equals energy-flux divergence). However, averaging transient near-inertial motions over an inertial period smooths, but does not eliminate, the energy tendency terms.

These energy balances hold for the decomposed equations of motion presented above. However, the forced motion and wave response are not orthogonal, so the total energy equation contains additional cross terms. The importance of these cross terms is a matter of perspective. Here we ignore them because they do not provide useful information about the wave response. For example, an oscillating wind stress does work directly on the waves (i.e., $\boldsymbol{\tau}\cdot\mathbf{u}'$), but, on average, this work is balanced by energy-flux divergence associated with the cross terms (i.e., $\overline{\mathbf{u}}p'$), so we ignore both terms.

3. Forced dynamics

a. Solution

Defining the complex number, $Z(t) = \overline{U} + i\overline{V}$, allows us to rewrite (8a) as

$$\frac{dZ}{dt}+(r+if)Z=T, \tag{11a}$$

or

$$\frac{d^2Z}{dt^2}+2r\frac{dZ}{dt}+(f^2+r_n^2)Z=\left(\frac{d}{dt}+r-if\right)T, \tag{11b}$$

where $T = \tau_x + i\tau_y$. The second form of the equation emphasizes that the system is a damped forced harmonic oscillator with natural frequency $\omega_0 = \mathrm{sgn}(f)\sqrt{f^2+r^2}$, damped frequency f, and quality factor $Q = |f|/(2r)$. A large quality factor indicates a weakly damped system prone to sharp resonance. Specifically, the quality factor is related to the bandwidth of the resonant peak by $\Delta\omega \approx |f|/(2Q) = r$. In the time domain, an unforced oscillation decays by a factor of e after $2Q$ radians. At midlatitude, mixed layer inertial oscillations have Q = 10–20, consistent with damping time scales of r^{-1} = 2–5 days.[1]

Defining the Fourier and inverse Fourier transforms as

$$\hat{Z}(\omega)=\int_{-\infty}^{\infty}Z(t)e^{-i\omega t}\,dt, \tag{12a}$$

$$Z(t)=\frac{1}{2\pi}\int_{-\infty}^{\infty}\hat{Z}(\omega)e^{i\omega t}\,d\omega, \tag{12b}$$

respectively, the transfer function for (11a) or (11b) is (Alford 2003)

$$\frac{\hat{Z}}{\hat{T}}=\frac{r-i(f-\omega)}{r^2+(f-\omega)^2}. \tag{13}$$

The function is asymmetric with respect to the origin and has a resonant peak at f, but not $-f$. The resonant frequency is slightly higher than that of a prototypical forced oscillator because the right-hand side of (11b) includes a time derivative. Increasing the damping flattens the resonant peak and lowers Q.

The Laplace transform,

$$\mathcal{L}[Z(t)]=\int_0^{\infty}Z(t)e^{-st}\,dt=\mathcal{Z}(s), \tag{14}$$

yields $Z(t)$ directly from the time series of recent wind stress. Substituting $s = i\omega$ in (13) leads to the Laplace transfer function

$$\frac{\mathcal{Z}(s)}{\mathcal{T}(s)}=\frac{(s+r)-if}{(s+r)^2+f^2}, \tag{15}$$

where we have assumed zero initial velocity and acceleration (i.e., $Z = 0$ and $dZ/dt = 0$ at $t = 0$). The "weight function" is the inverse transform of the transfer function,

$$W(t)=\mathcal{L}^{-1}[\mathcal{Z}(s)/\mathcal{T}]=e^{-(r+if)t}. \tag{16}$$

Since $\mathcal{Z}(s) = \mathcal{W}(s)\mathcal{T}(s)$ is now the product of two functions with known inverse transforms $[W(t), T(t)]$, the Laplace transform convolution theorem yields

$$Z(t)=\int_0^t W(t')T(t-t')\,dt', \tag{17}$$

where t' is a time lag. This integral weights the previous wind measurements to provide an optimal estimate of the present transport. The weight of the wind measurements

[1] For reference, Carwright and Ray (1991) reported similar quality factors for the M_2 barotropic tide, but see also Garrett and Munk (1971).

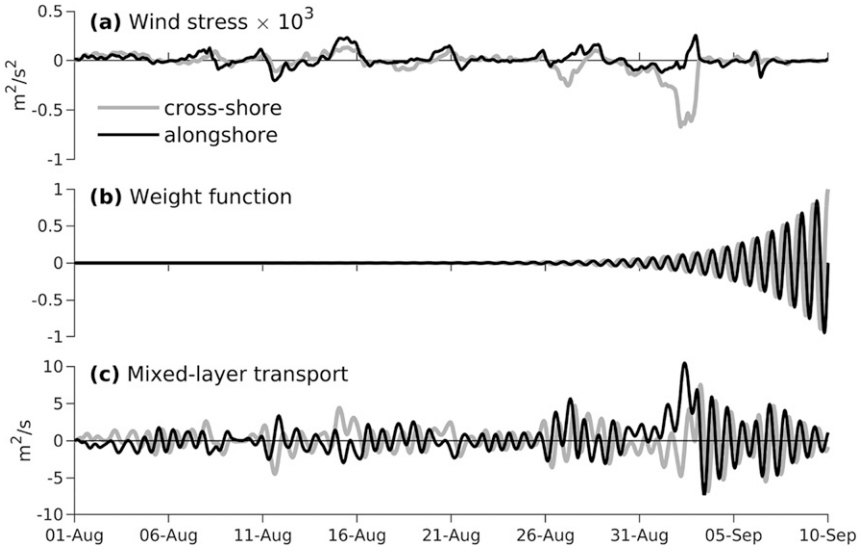

FIG. 2. (a) NOGAPS wind stress on the New Jersey shelf during 2006. (b) The weight function is reversed on the time axis to illustrate how past winds are weighted in the calculation of transport on 10 Sep. (c) Mixed layer transport occurs over a depth of $H_{\text{mix}} \approx 10$ m.

decreases exponentially as the time lag increases (the e-folding time is $1/r$) and oscillates at the inertial frequency, so bursts of wind may either reinforce or diminish preexisting velocities depending on their precise timing and duration. Steady winds produce weak time-averaged velocities because they are multiplied by both positive and negative weights. Using the standard properties of Laplace transforms, these solutions are easily extended to account for preexisting velocities, which are sometimes crucial for explaining observations (Plueddemann and Farrar 2006).

b. Application to the New Jersey shelf

The above solution provides an estimate of mixed layer transport on the New Jersey shelf during the Shallow Water 2006 experiment (SW06; see Tang et al. 2007) using wind stress from the Navy Operational Global Atmospheric Prediction System (NOGAPS; hycom.org; Fig. 2). Between 1 August and 10 September 2006, wind stress reaches a maximum value of about 0.5 Pa during Tropical Storm Ernesto on 3 September (Fig. 2a). Mixed layer transports, computed from (17) with an inertial period of about 19 h (for 39°N), and a drag parameter of $r^{-1} = 3.5$ days (a reasonable value, but see Plueddemann and Farrar 2006), are near-inertial and reach about $10\,\text{m}^2\,\text{s}^{-1}$ during the storm (Fig. 2c).

The frequency-domain solution reveals that the mixed layer response to near-inertial wind stress is amplified by the peak in the transfer function, which imparts a distinct inertial peak in the transport spectrum (Fig. 3). However, wind stress Fourier coefficients are an order of magnitude larger at low frequencies than the inertial frequency, so low-frequency transport is also substantial despite being nonresonant.

4. Wave dynamics

a. Solution

Here we consider waves generated at a vertical-wall coastline at $x = 0$ in the absence of alongshore variability ($\partial/\partial y = 0$). If wind stress and f are horizontally uniform, open-ocean forcing due to $\overline{w}_n$ is negligible and (8b) and (8c) can be written as unforced Klein–Gordon equations (e.g., Llewellyn Smith and Young 2002):

$$\frac{\partial^2 u_n'}{\partial t^2} + f^2 u_n' = c_n^2 \frac{\partial^2 u_n'}{\partial x^2}, \tag{18a}$$

$$\frac{\partial^2 p_n'}{\partial t^2} + f^2 p_n' = c_n^2 \frac{\partial^2 p_n'}{\partial x^2}, \tag{18b}$$

which are also known as "equations of telegraphy" (Cahn 1945) or the equations for an "elastically supported string" (Morse 1948).

The no-normal-flow condition at the coast forces the waves by requiring $u_n' = -\overline{u}_n$ at $x = 0$, where $\overline{u}_n = \overline{U}\phi_n|_0/H$. For pressure, this condition becomes

$$\frac{\partial^2 \overline{u}_n}{\partial t^2} + f^2 \overline{u}_n = \frac{\partial^2 p_n}{\partial x \partial t} \quad \text{at} \quad x = 0. \tag{19}$$

A second set of boundary conditions also requires that waves propagate offshore or decay away from the coast.

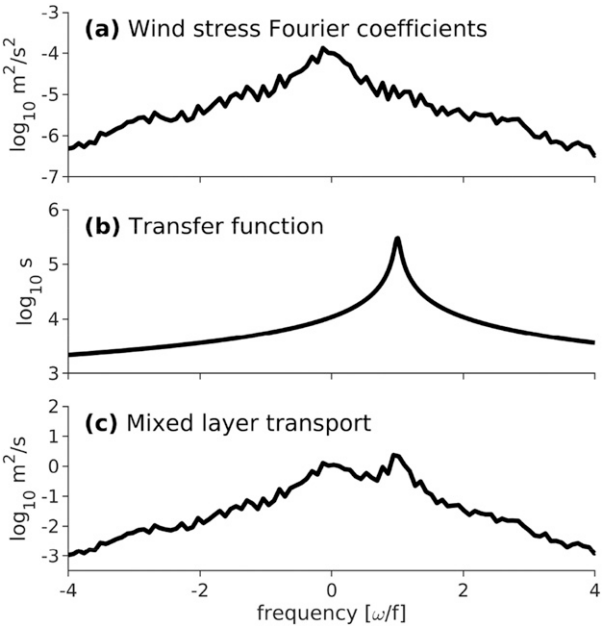

FIG. 3. (a) Wind stress Fourier coefficients are multiplied by the (b) transfer function to produce the (c) transport coefficients. The Fourier coefficients have a spectral width of $\Delta f = f/12$ and are complex, but only their absolute value is plotted. Fourier coefficients are plotted to emphasize the simple algebraic relationship in the frequency domain between wind stress, the transfer function, and transport. Conventional plots of power spectral density would have sharper inertial peaks.

Fourier transforming the Klein–Gordon equations in time reduces them to second-order ordinary differential equations in x,

$$-\alpha^2\frac{\omega^2}{c_n^2}\hat{u}'_n = \frac{\partial^2\hat{u}'_n}{\partial x^2}, \tag{20a}$$

$$-\alpha^2\frac{\omega^2}{c_n^2}\hat{p}'_n = \frac{\partial^2\hat{p}'_n}{\partial x^2}, \tag{20b}$$

where the parameter $\alpha = \sqrt{1 - f^2/\omega^2}$ quantifies the role of rotation. The inverse transformed solutions to (20) are

$$u'_n(x,t) = -\frac{1}{2\pi}\int_{-\infty}^{\infty}\overline{u}_n e^{i(k_n x-\omega t)}\,d\omega, \tag{21a}$$

$$p'_n(x,t) = -\frac{1}{2\pi}\int_{-\infty}^{\infty}c_{g,n}\overline{u}_n e^{i(k_n x-\omega t)}\,d\omega, \tag{21b}$$

where $k_n = \alpha\omega/c_n$ is the wavenumber, and $c_{g,n} = \alpha c_n$ is the group speed. The solution comprises offshore propagating waves ($|\omega| > |f|$) and coastally trapped motions ($|\omega| < |f|$) when α is real or imaginary, respectively.

The Laplace transform yields the wave response directly from the recent time series of mixed layer transport. The Laplace transfer functions,

$$\frac{\mathcal{U}_n(s)}{\overline{\mathcal{U}}_n} = -e^{-\sqrt{s^2+f^2}x/c_n}, \tag{22a}$$

$$\frac{\mathcal{P}_n(s)}{\overline{\mathcal{U}}_n} = -\frac{\sqrt{s^2+f^2}}{s}e^{-\sqrt{s^2+f^2}x/c_n}, \tag{22b}$$

are found by Laplace transforming the wave equation (18), solving the second-order differential equation in x and applying the boundary conditions. The inverse transforms of the transfer functions are the weight functions (nondimensionalized by dividing by f)

$$W^u(t^*,x^*) = -\delta(t^*-x^*) + x^*\frac{J_1(\sqrt{t^{*2}-x^{*2}})}{\sqrt{t^{*2}-x^{*2}}}, \tag{23a}$$

$$W^p(t^*,x^*) = -\delta(t^*-x^*) + t^*\frac{J_1(\sqrt{t^{*2}-x^{*2}})}{\sqrt{t^{*2}-x^{*2}}} - \int_{x^*}^{t^*}J_0(\sqrt{t'^{*2}-x^{*2}})\,dt'^*, \tag{23b}$$

where δ is the Dirac delta, nondimensional time and distance are $t^* = ft$ and $x^* = x/\lambda_n$, respectively, and the Rossby radius is $\lambda_n = c_n/f$. The weight functions are zero when $t^* < x^*$, and J_m is the mth-order Bessel function of the first kind. Velocity and pressure are the convolutions,

$$u'_n(x,t) = \int_0^t fW^u(ft',x/\lambda_n)\,\overline{u}_n(t-t')\,dt', \tag{24a}$$

$$p'_n(x,t) = c_n\int_0^t fW^p(ft',x/\lambda_n)\,\overline{u}_n(t-t')\,dt'. \tag{24b}$$

The Dirac deltas in the weight functions provide the classical solution to the nondispersive wave equation, which describe disturbances that retain their shape as they propagate offshore at speed c_n.

The second term in each of the weight functions accounts for dispersion due to rotation, which stretches the wave as it propagates away from the coast. These terms are zero until the nondispersive wavefront arrives, at $t = x/c_n$, and decay rapidly after.

The last term in W^p is associated with coastal upwelling. This integral converges to a nonzero constant at long lags near the coast (i.e., large t and small x), so the complete history of wind forcing determines the pressure associated with coastal upwelling. Numerical evaluation of this integral confirms that the e-folding distance of coastal upwelling is the Rossby radius, that is,

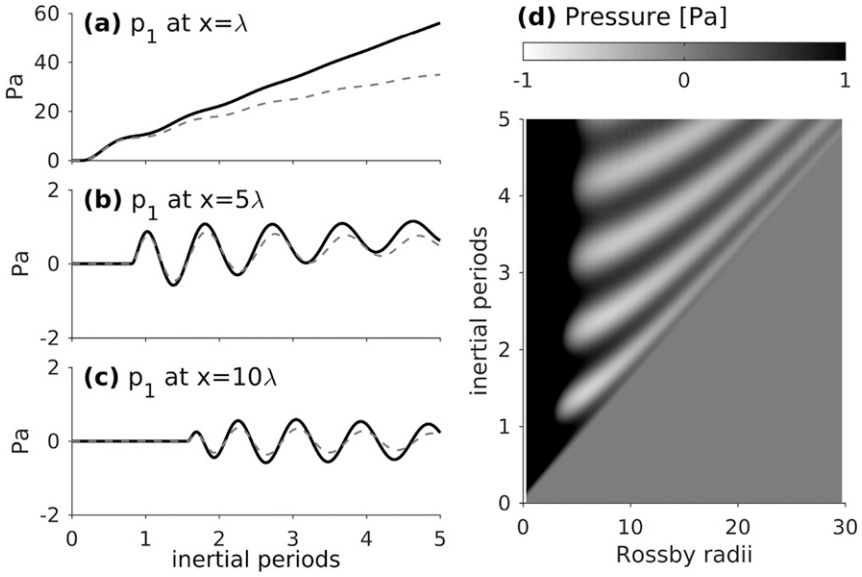

FIG. 4. (a)–(c) The mode-1 pressure response to a sudden alongshore wind is computed from (24b) (solid) and (12) from Kundu et al. (1983) (dashed) at different distances from shore. (d) The full solution consists of increasing upwelling at the coast and offshore propagating waves that are bounded by a front traveling at the nonrotating wave speed. This solution uses $\boldsymbol{\tau} = 0.1\hat{\mathbf{j}}$ Pa, $f = 10^{-4}\,\mathrm{s}^{-1}$, $H = 250$ m, $H_{\mathrm{mix}} = 25$ m, $N = 10^{-2}\,\mathrm{s}^{-1}$, and $c_1 = 0.78\,\mathrm{m\,s}^{-1}$. Viscosity in Kundu et al.'s (1983) solution is $\nu = 0.02\,\mathrm{m}^2\,\mathrm{s}^{-1}$, which is equivalent to $r^{-1} = 3.5$ days.

$$\lim_{t^*\to\infty}\int_{x^*}^{t^*} J_0\left(\sqrt{t'^{*2}-x^{*2}}\right)dt'^{*} = e^{-x/\lambda_n}. \tag{25}$$

The solutions given by (24) are equivalent to those derived by Kundu et al. (1983), except that they (i) apply to arbitrary time series of wind stress instead of a sudden impulse and (ii) incorporate mixed layer damping rather than a vertical viscosity that applies to all components of the flow. The solutions are identical for the inviscid response to a sudden wind, but, for the same equivalent damping, the wave pressure computed here is slightly larger than that of Kundu et al. (1983) (Fig. 4). In practice, both dissipative parameterizations are overly simplified to allow analytical solutions, so it is sensible to select the parameterization most convenient for a desired application.

A Hovmöller diagram of pressure illustrates both the coastal-trapped response and offshore propagating waves (Fig. 4d), indicating that C_w contributes to both a positive nearshore energy tendency and flux divergence associated with offshore wave radiation. The offshore radiating wave is bounded by a front moving at the nonrotating wave speed. Waves with slower group speeds trail the front, but have faster phase speeds (i.e., flatter slopes), consistent with the inertio-gravity dispersion relation. If alongshore variability were introduced, the coastal-trapped response would propagate as a Kelvin wave, but this does not occur in our idealized model.

Wave dispersion makes it challenging to predict waves far from shore. As the waves in the front separate, they reveal the detailed structure of the front. As a result, high *temporal* resolution boundary forcing is required to specify the solution far from the coast. To see this, note that the deformation terms depend on $J_1(\zeta)/\zeta$, where $\zeta = \sqrt{t^{*2}-x^{*2}}$. Because $J_1(\zeta)/\zeta$ is periodic and decays rapidly as t^* increases, accurate solutions should resolve $J_1(\zeta)$ with a minimum of, say, 20 boundary forcing measurements between its first and third zeros (which are spaced by $\Delta\zeta \approx 6.3$). Thus the boundary forcing (i.e., wind) should have at least

$$N_s = 20 \times 2\pi \Big/ \left(\sqrt{\Delta\zeta^2 + x^{*2}} - x^{*}\right) \tag{26}$$

measurements per inertial period. At the coast $N_s = 20$, at $x^* = 10$ Rossby radii $N_s = 70$, and at $x^* = 100$ Rossby radii $N_s = 634$ measurements. Therefore, along coastlines where only hourly wind data are available, radiated near-inertial waves can only be accurately specified a few Rossby radii from the coast. Attempts to predict waves at great distances will generate noise by aliasing the weight functions.

b. *Application to the New Jersey shelf*

The above solution provides estimates of wave velocity, pressure, and energy flux on the New Jersey shelf during the SW06 experiment (Fig. 5). The solution

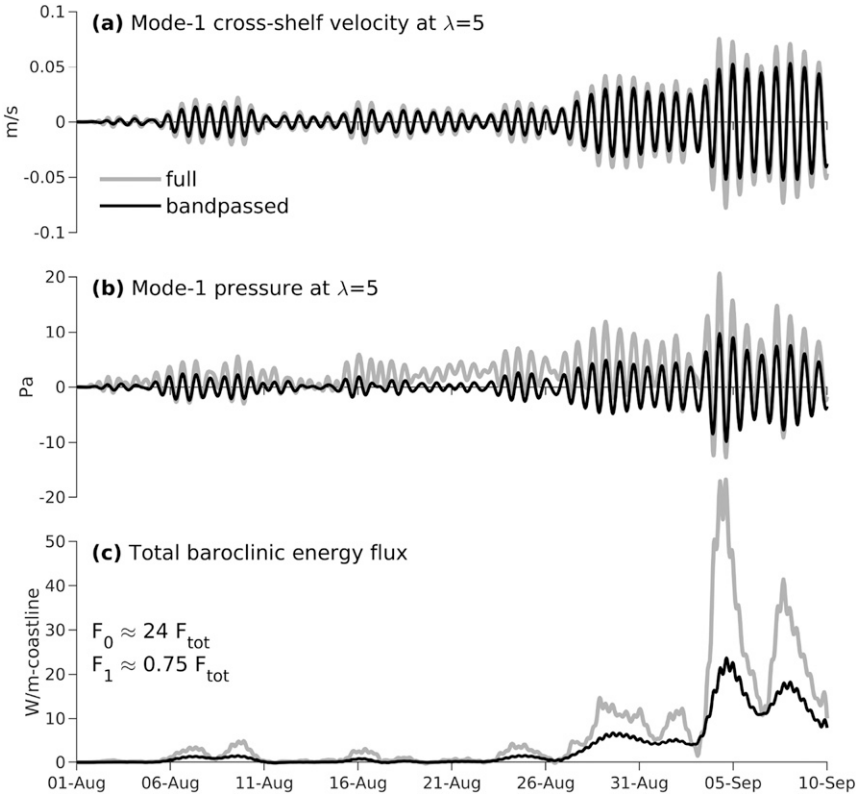

FIG. 5. Wind stress during the SW06 experiment is used to estimate the (a) velocity and (b) pressure of a mode-1 wave generated at the coast (approximated as a vertical wall with $H = 62.5$ m). (c) The baroclinic offshore energy flux $F_{\text{tot}} = \sum_{n=1}^{\infty} F_n$ (smoothed over an inertial period using a 19-h moving average) is estimated at five Rossby radii ($x^* = 5$) from the coast to ensure coastal-trapped signals have decayed. The barotropic (mode 0) energy flux F_0 (not shown) is about 50 times larger than F_{tot} because mode 0 has a much larger eigenspeed. The mode-1 energy flux F_1 (not shown) accounts for 70% of the total baroclinic energy flux F_{tot}. Band passing the velocity and pressure between $0.8f$ and $1.2f$ slightly reduces their variance and decreases energy flux by about 50%.

utilizes $H = 62.5$ m and observed stratification (Nash et al. 2012a) with $H_{\text{mix}} = 10$ m. The solutions to the vertical-mode eigenvalue problem (5) are constant in the mixed layer and nearly sinusoidal below [Fig. 6; see Kelly (2016) for the numerical method]. The eigenspeeds decrease rapidly with increasing mode number (i.e., $c_0 = 24.8\,\text{m s}^{-1}$, $c_1 = 0.52\,\text{m s}^{-1}$, etc.).

To isolate radiating waves and eliminate coastal-trapped signals, mode-1 velocity and pressure are computed at $x^* = 5$ Rossby radii from the coast (Fig. 5). Wave velocities are about $0.05\,\text{m s}^{-1}$ and wave pressure is about 5 Pa. Note that although mixed layer velocity estimates are 0.5–1 m s^{-1} during Ernesto (section 3b), the mode-1 velocities only reach about $0.05\,\text{m s}^{-1}$, because the mixed layer current projects onto many modes (recall $\overline{u}_n = \overline{U}\phi_n|_0/H$). Velocity and pressure are in phase, so they produce an offshore (positive) energy flux that is briefly greater than 50 W (m coastline)$^{-1}$ (Fig. 5c).

Bandpass filtering is another method of isolating near-inertial waves. We use a Morlet wavelet transform with 16 voices per octave (see Johnston et al. 2015) to isolate signals between $0.8f$ and $1.2f$. Even at $x^* = 5$ velocity and pressure have a small low-frequency component that is removed by the bandpass filter. The filter also slightly attenuates the near-inertial oscillations and reduces energy flux to about half the raw values (Fig. 5).

Mode-1 pressure spectra clearly separate the coastal-trapped and radiating wave responses (Fig. 7). The pressure response at subinertial frequencies decreases by two orders of magnitude within $x^* = 5$ Rossby radii of the coast. Conversely, the superinertial response is identical at all distances from the coast. At the inertial frequency, a peak in the mixed layer spectrum and valley in the transfer function leads to a relatively smooth (unpeaked) pressure spectrum. The slow roll-off of superinertial pressure leads to significant energy

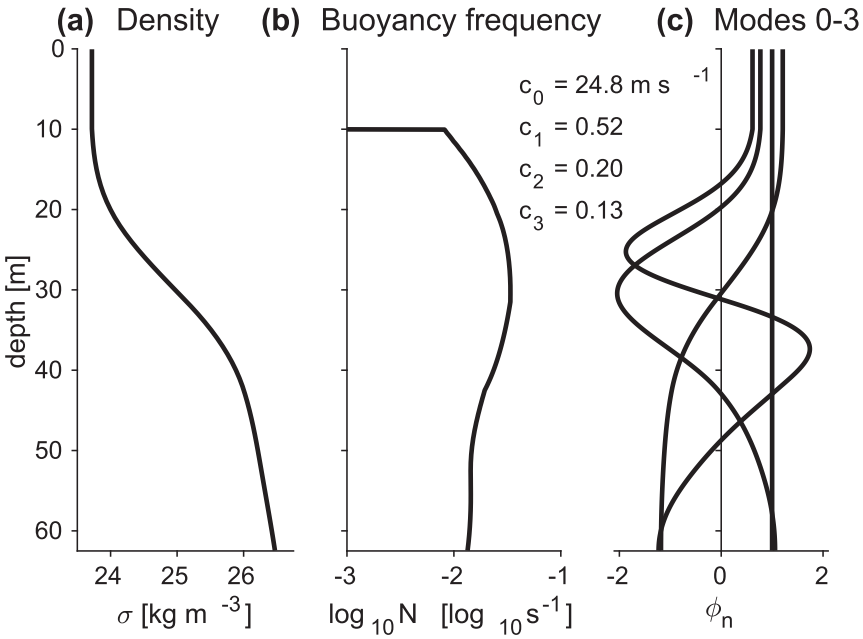

FIG. 6. The observed profiles of (a) potential density and (b) stratification determine the vertical modes and (c) eigenspeeds. The mixed layer depth varied throughout the SW06 experiment, but here we set $N^2 = 0$ to a depth of $H_{\text{mix}} = 10$ m.

flux out to about $2f$, explaining why signals bandpassed between $0.8f$ and $1.2f$ only capture half of the total energy flux. Unfortunately, the spectrum between f and $2f$ is usually contaminated by nonstationary tides in the coastal ocean (Nash et al. 2012b), so total energy flux is typically unmeasurable. In this regard, observations of near-inertial motions where tides are small, such as in the Laurentian Great Lakes, are easier to analyze (Choi et al. 2012; Austin 2013).

The depth-dependent velocity and pressure are the sums of the modal solutions. Snapshots of these fields reveal a downward propagating internal-wave beam emanating from the coast (Fig. 8). These images emphasize that CNIW generation is a mechanism that transports energy from the surface mixed layer to the stratified interior, where it may drive diapycnal mixing, sediment resuspension, etc.

5. Effects of cross-shore bathymetry

Most coastal bathymetry shoals gradually and is poorly approximated by a vertical wall. In these locations, the bottom shoals until it reaches the base of the mixed layer, at which point the water is, by definition, unstratified, and surface waves (i.e., barotropic waves or mode-0 waves) are the only possible response to convergences in mixed layer transport. Thus, mode-0 waves radiate offshore. As these waves propagate to deeper stratified water they conserve transport (in the long-wave limit) and, like surface tides, scatter over topographic bumps. Hopkins et al. (2014) qualitatively discussed near-inertial topographic internal-wave generation, but the process, to our knowledge, has not been examined in detail.

a. *Numerical simulations*

The standard expression for topographic internal-wave generation is (Kelly 2016)

$$C_T = -\sum_{n=1}^{\infty} \nabla H \cdot \mathbf{u}_0' p_n' \phi_n|_{-H}, \tag{27}$$

although it has not been previously applied to near-inertial waves. In practice, it is difficult to observe the mode-0 wave velocity because it destructively interferes with the mode-0 mixed layer velocity within a fraction of an inertial period (Shearman 2005). However, the mode-0 wave response can be simulated using two techniques:

1) One can run a realistic simulation with observed wind forcing and topography, and a ''twin'' simulation with observed wind forcing and a deep flat bottom (with open boundaries). Subtracting the flat-bottom solution from the realistic solution isolates the topographically induced component of the flow (i.e., the coastal response). Hall et al. (2013) used a similar technique to separate incident and reflected internal waves at a topographic slope.

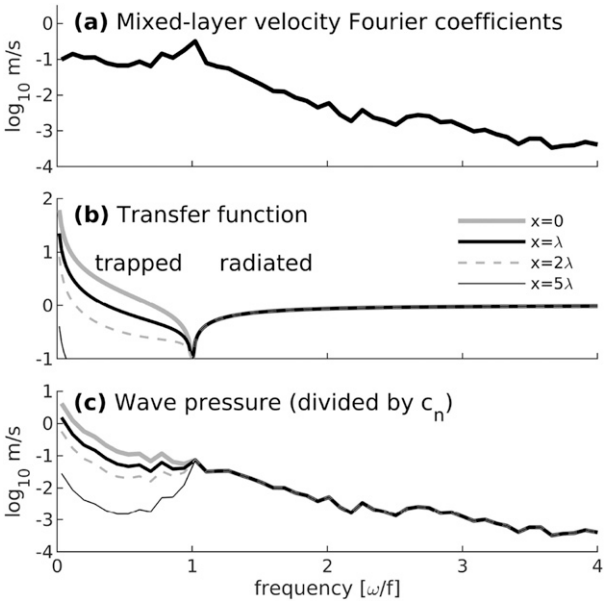

FIG. 7. (a) Mode-1 mixed layer velocity Fourier coefficients are multiplied by (b) the transfer function to produce (c) the pressure coefficients. Subinertial pressure coefficients decrease with distance offshore, but superinertial coefficients are unaffected (all of the lines overlap). The Fourier coefficients have a spectral width of $\Delta f = f/12$ and are complex, but only their absolute value is plotted.

2) One can estimate the flat-bottom response using a slab model, and then simulate the coastal response by prescribing the mode-0 boundary transports. In this case, the coastal wall is replaced with an open boundary (i.e., we truncate the New Jersey shelf at the 62.5-m isobath). This technique is analogous to boundary-forced simulations of internal-tide generation.

To quantify the effect of cross-shore bathymetry, the MIT general circulation model (MITgcm; Marshall et al. 1997) simulated near-inertial topographic internal-wave generation at the New Jersey Shelbreak using techniques 1 and 2. Bathymetry and stratification were identical to Nash et al. (2012a), except that the depth of the abyss was truncated at 1000 m. The resolution was $\Delta z = 2$ m, and $\Delta x = 250$ m in the region of interest, but telescoped to $\Delta x = 5$ km at the offshore boundary. A flow-relaxation condition at the open boundaries prevented the reflection of outgoing internal waves. Horizontal and vertical eddy viscosities of $10^{-2}\,\mathrm{m^2\,s^{-1}}$ and $10^{-3}\,\mathrm{m^2\,s^{-1}}$, respectively, stabilized the simulations. The first two simulations were forced with observed wind stress and either observed topography or a flat bottom, in accordance with technique 1. The third simulation was forced by the barotropic (mode 0) wave transport [computed from Eq. (24a)] prescribed at the open boundaries, in accordance with technique 2.

Techniques 1 and 2 produces nearly identical flows for the first few inertial periods (not shown), but the solutions eventually diverged because technique 1 exhibited nonlinear responses during strong wind and allowed standing waves to develop between the coast and shelfbreak. Only the results of technique 2, which cleanly isolate topographic internal-wave generation at the shelfbreak, are further examined.

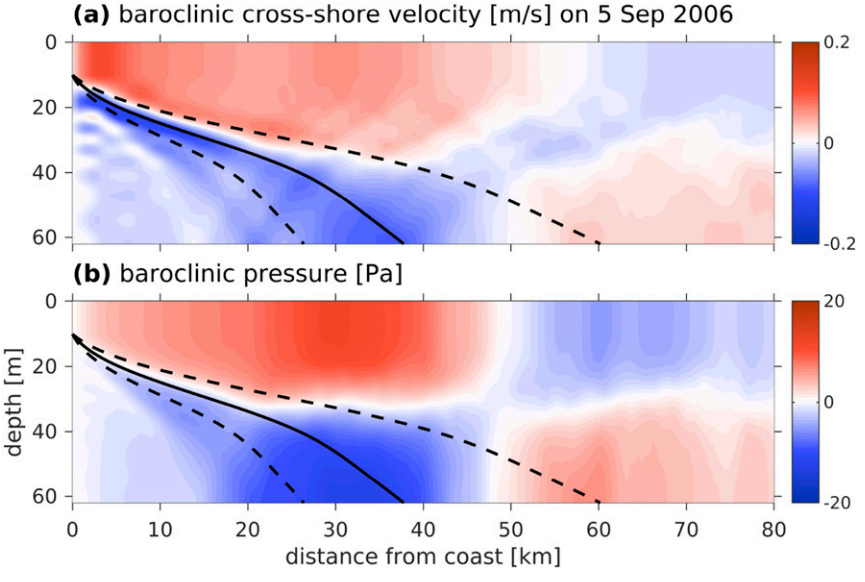

FIG. 8. Summing the modal wave solutions produces the (a) depth-dependent velocity and (b) pressure fields. Both fields are bandpassed between $0.8f$ and $1.2f$. Rays are drawn for frequencies $1.02f$, $1.05f$ (solid) and $1.10f$.

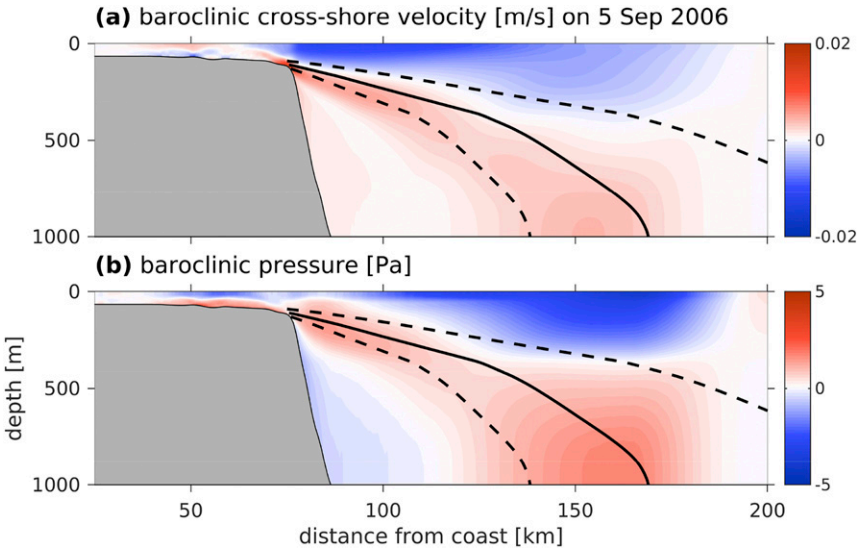

FIG. 9. Snapshots of bandpassed (a) cross-shore velocity and (b) baroclinic pressure from the MITgcm simulations forced using technique 2 in section 5. The fields show internal wave beams emanating from the shelfbreak. Rays are drawn for frequencies 1.02*f*, 1.05*f* (solid), and 1.10*f*.

The third simulation, which employed technique 2, was integrated for 40 days starting on 1 August 2006. Snapshots of bandpassed velocity and pressure on 5 September indicate internal-wave generation at the shelfbreak reminiscent of internal-tide generation (Fig. 9), but less energetic (near-inertial and semidiurnal transports are 4 and 20 $\mathrm{m^2\,s^{-1}}$, respectively; cf. Fig. 10a and Zhang and Duda 2013). Part of the baroclinic response is also subinertial (not shown) and, therefore, trapped to the shelfbreak because the mode-0 velocity forcing contains both sub- and superinertial frequency content (i.e., it is a combination of trapped and radiating mode-0 waves).

Bandpassed topographic conversion at the shelfbreak approximately balanced offshore near-inertial energy flux in the simulation (Fig. 10c). Energy flux was $\mathcal{O}(1)$ W (m coastline)$^{-1}$, except for a brief period right after Ernesto, when C_T reached 10 W (m coastline)$^{-1}$ (Fig. 10c). Even after doubling the energy flux to account for signal attenuation by the bandpass filter, the brief increase associated with Ernesto is still an order of magnitude weaker than local semidiurnal internal-tide generation (Nash et al. 2012a; Zhang and Duda 2013; Kelly and Lermusiaux 2016). Furthermore, C_T is less than the mode-1 energy flux predicted for a vertical-wall coastline at $H = 62.5$ m [50 W (m coastline)$^{-1}$; Fig. 5c].

b. *Observations at the New Jersey shelfbreak*

Numerous moorings were deployed during SW06 that revealed strong tidal and near-inertial variability (see Tang et al. 2007; Shroyer et al. 2011; Nash et al. 2012a). We analyzed sparse, but nearly full-depth, measurements of temperature, salinity, and velocity at four shelf moorings (SW29, SW30, SW32, and SW34) and three shelfbreak moorings (SW40, SW42, and SW43). The moorings are described in detail by Shroyer et al. (2011) and Nash et al. (2012a).

Near-inertial velocities were highly coherent at all seven moorings, suggesting a spatially uniform slab-like response to local wind forcing (Shroyer et al. 2011). An estimate of mixed layer transport is needed to compare the observations with a slab model. The integral of velocity from the base of the mixed layer to the surface is the simplest estimate of mixed layer transport. Unfortunately, near-surface velocity observations are lacking and the moorings have insufficient vertical resolution to determine the precise depth of the mixed layer. A more robust estimate of mixed layer transport is $\overline{\mathbf{U}} = \overline{\mathbf{u}}_1 H/\phi_1|_0$, which relies on better-observed quantities: the mode shape ϕ_1, bottom depth H, and the mode-1 velocity amplitude

$$\overline{\mathbf{u}}_1 = \frac{1}{H}\int_{-H}^{0} \overline{\mathbf{u}}(z)\phi_1(z)\,dz\,. \tag{28}$$

Mixed layer transport at SW43 ($H = 480$ m) and that predicted by (17) using NOGAPS wind stress have similar character, but do not have identical amplitude and phase, except around 25 August (Fig. 10a). Uncertainty in the wind stress alone can explain the disagreement. Theoretical transports computed from wind at regional NDBC buoys 44004 and 44009 (not shown)

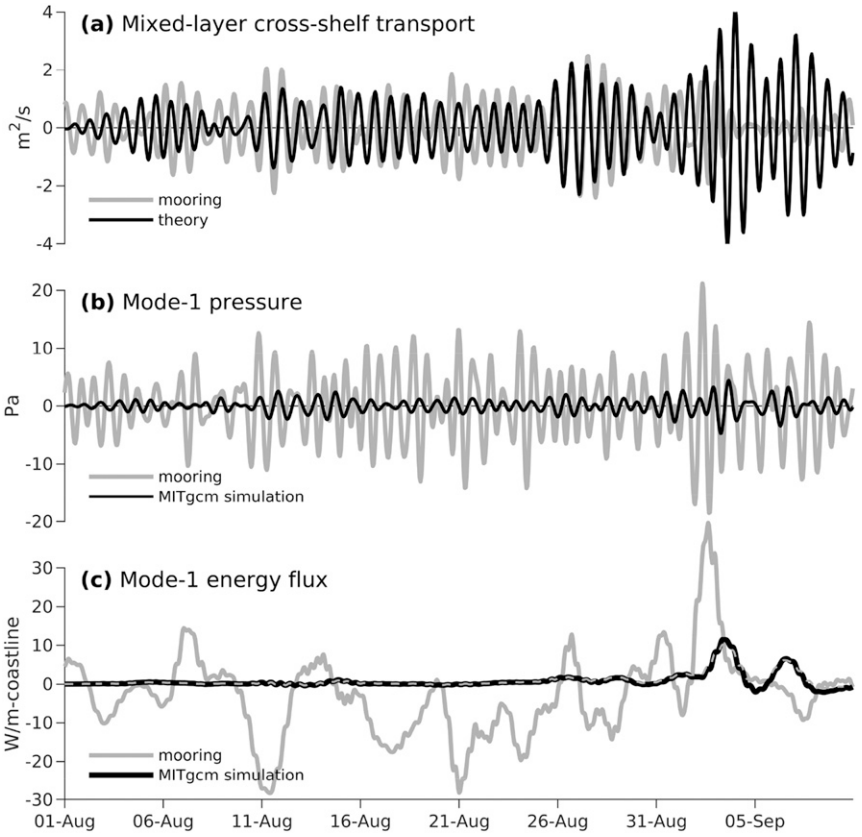

FIG. 10. (a) Observed (gray) and predicted (black) mixed layer transport during SW06. (b) Observed (gray) and simulated (black) mode-1 pressure at the New Jersey Shelfbreak (H = 480 m). The observations are from the SW43 mooring. All signals are bandpassed between 0.8f and 1.2f. (c) Observed (gray) and simulated (black) mode-1 energy flux (smoothed over an inertial period using a 19 h moving average). Simulated topographic internal-wave generation C_T (dashed gray) in (c) is indistinguishable from simulated energy flux.

differed from each other and the observed transport, indicating that wind stress in the near-inertial band is not spatially coherent enough to predict mixed layer transports more than a few tens of kilometers from a wind station. This finding directly contradicts our assumption of spatially uniform wind stress and implicates a mechanism for open-water near-inertial wave generation that is neglected in our analysis.

Mode-1 pressure at the farthest offshore mooring (SW43, H = 480 m) was estimated from temperature and salinity following Waterhouse et al. (2018). Observed mode-1 pressure was about 10 Pa, while mode-1 pressure in the MITgcm simulation was only 3 Pa (Fig. 10b). Therefore, topographic generation at the shelfbreak cannot explain all observed near-inertial pressure. Additional sources of near-inertial pressure could be CNIWs propagating out from the coast (section 4), near-inertial waves generated in open-water by offshore storms, or nonstationary internal tides leaking into the inertial band. Observations of offshore energy flux after Ernesto suggest CNIWs (cf. Figs. 5c and 10c), while observations of onshore energy flux during August suggest onshore propagating internal tides (see Nash et al. 2012a; Kelly et al. 2016).

6. Global relevance

The preceding sections show that wind work in the mixed layer can be transferred to offshore propagating near-inertial waves. In most locations, gently sloping coastal bathymetry only facilitates barotropic wave generation at the coast, but these waves can scatter into internal waves as they propagate over topographic features in deeper stratified water. Regardless of how much scattering occurs, the barotropic wave accounts for nearly all of the offshore energy flux, that is, the calculations in section 4b indicate that the barotropic (mode 0) energy flux F_0 is 50 times the baroclinic flux (Fig. 5). Here, we make a global estimate of the offshore mode-0 energy flux.

Using the Fourier transfer function (13), the time-averaged rate of work is

$$P = \frac{\rho_0}{2\pi H_{\text{mix}}} \int_{-\infty}^{\infty} S_{TT}(\omega) \frac{r}{r^2 + (f-\omega)^2} d\omega, \tag{29}$$

where $S_{TT}(\omega)$ is the power spectral density of wind stress and the factor of 2π arises from Parseval's theorem. Changing the variable of integration to $\gamma = (\omega - f)/r$ yields

$$P = \frac{\rho_0}{2\pi H_{\text{mix}}} \int_{-\infty}^{\infty} S_{TT}(f + r\gamma) \frac{1}{1+\gamma^2} d\gamma. \tag{30}$$

As r goes to zero, the transfer function behaves like a Dirac delta (multiplied by π), so that only near-inertial wind stress contributes to the integral. The wind work becomes

$$P \approx \frac{\rho_0}{2H_{\text{mix}}} S_{TT}(f) (\text{W m}^{-2}). \tag{31}$$

Perhaps surprisingly, this approximate formula only depends on near-inertial wind stress, and is independent of both the inertial frequency and linear damping coefficient (i.e., quality factor). Previous studies have also noted that r has little effect on wind work, provided $r \ll |f|$ (e.g., Alford 2003; Jing et al. 2017).

The depth-integrated time-averaged mode-0 energy flux radiated to deep water is

$$F_0 = \frac{\rho_0}{2\pi H} \int_{|f|}^{\infty} c_{g,0} [S_{ZZ}(-\omega) + S_{ZZ}(\omega)] \, d\omega, \tag{32}$$

where $S_{ZZ}(\omega)$ is the power spectral density of the cross-shore mixed layer transport and both positive and negative frequencies contribute to energy flux. Even though barotropic waves originate where the mixed layer touches the bottom, (32) provides an estimate of the energy flux radiated to the deep ocean (i.e., to an offshore depth H), because barotropic transport is conserved in the long-wave limit. The H^{-1} dependence in (32) indicates that offshore energy flux decreases with depth because the offshore-propagating wave is partially reflected as the wave speed increases.

The calculation of F_0 only depends on cross-shore transport, but if the near-inertial wind stress is approximately isotropic, then

$$S_{ZZ}(\omega) \approx \frac{1}{2} S_{TT}(\omega) \frac{1}{r^2 + (f-\omega)^2}. \tag{33}$$

The transfer function is asymmetric and only peaked at $\omega = f$, so depending on the sign of f, either $S_{ZZ}(-\omega)$ or $S_{ZZ}(\omega)$ can be neglected in (32). The group speed is approximated as $c_{g,0} \approx c_0 \sqrt{2(\omega - |f|)/|f|}$ for $\omega - |f| \ll |f|$ using the binomial expansion. Substituting the approximate expressions for $S_{ZZ}(\omega)$ and $c_{g,0}$ into (32), neglecting the nonpeaked side of the spectrum, and writing the integral in terms of $\gamma = (\omega - |f|)/r$ yields

$$F_0 \approx \frac{\rho_0}{4\pi H} \frac{c_0}{|f|} \sqrt{\frac{|f|}{r}} \int_0^{\infty} S_{TT}[f + \text{sgn}(f) r\gamma] \frac{\sqrt{2\gamma}}{1+\gamma^2} d\gamma. \tag{34}$$

Once again, the transfer function behaves like a Dirac delta (multiplied by π) as r goes to zero, leading to

$$F_0 \approx \frac{\sqrt{2}\rho_0}{4H} \lambda_0 \sqrt{Q} S_{TT}(f) [\text{W(m coastline)}^{-1}], \tag{35}$$

where $\lambda_0 = \sqrt{gH}/|f|$ is the barotropic Rossby radius and $Q = |f|/(2r)$ is the quality factor. Although the wave solution is inviscid, F_0 depends on damping (through the quality factor Q) because r alters the bandwidth of the forced velocities, which in turn alters the group speeds of the resulting waves (i.e., group speed is a sensitive function of ω around $\omega \approx f$).

The global energy flux due to CNIWs could be estimated by integrating (32) or (35) over the length of the coastline, but this length can vary by several orders of magnitude depending on the measurement precision (Mandelbrot 1967). Instead, we divide F_0 by P [the time-averaged rate of wind work; Eq. (31)] to determine the offshore extent of the coastal boundary zone D, where wind work is transferred to near-inertial waves

$$D = \lambda_0 \sqrt{\frac{Q}{2} \frac{H_{\text{mix}}}{H}} (\text{m}). \tag{36}$$

We then estimate the global flux by integrating the wind work that occurs where the local estimate of D is greater than the distance to the nearest coast.[2] The coastal boundary zone D is 10–500 km at midlatitudes in the deep ocean, where the barotropic Rossby radius is $\lambda_0 = 1500$–3000 km, the ratio H_{mix}/H is 0%–5%, and the near-inertial quality factor is $Q = 10$–20 (corresponding to damping time scales of $r^{-1} = 2$–5 days). As might be expected, the length scale D is in reasonable agreement with observations of the "coastal inhibition" of inertial oscillations (e.g., Shearman 2005).

Global wind work and CNIW flux are estimated between 2.5° and 60° latitude during 2014–15 using (31) and (36) with (i) 3-h winds on a 0.5° grid from the Navy Global Environmental Model (NAVGEM; hycom.org),

[2] The distance to the nearest coast converges with measurement precision, unlike the length of the coastline.

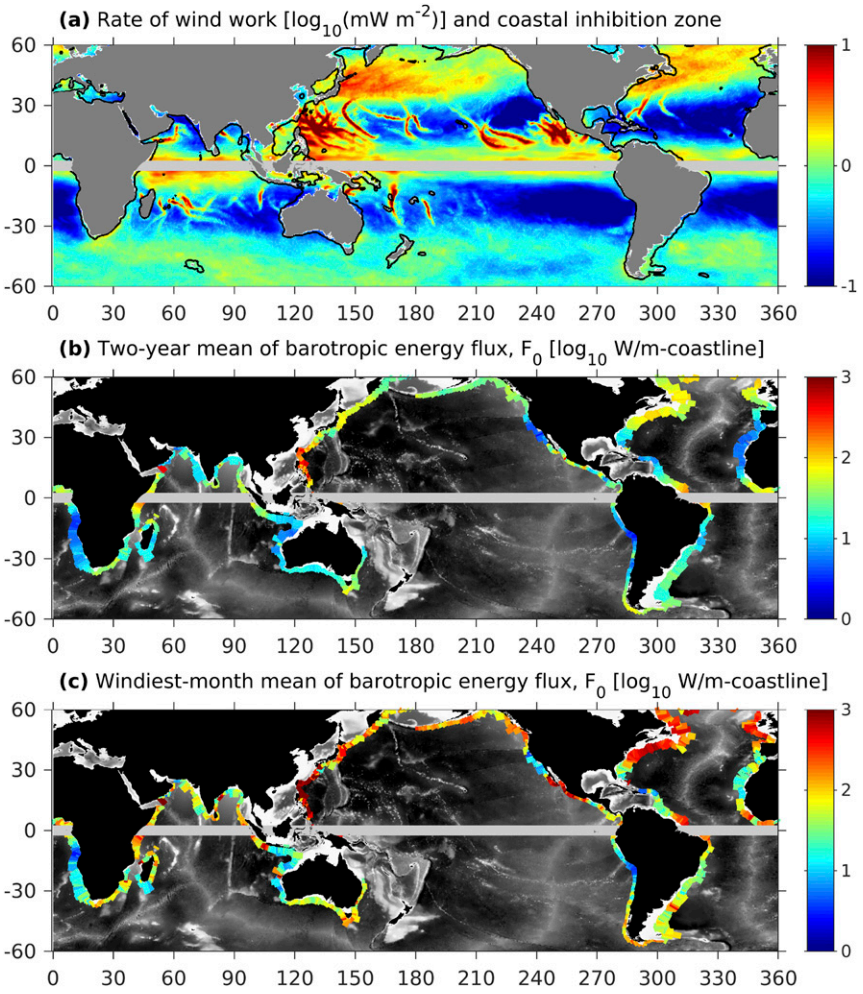

FIG. 11. (a) The average wind work P from 2014–15 NAVGEM winds has a global integral of 0.31 TW. Wind work within the coastal boundary region D is 0.03 TW (black line). (b) The 2-yr mean F_0 is typically less than 100 W (m coastline)$^{-1}$, while (c) the mean of F_0 over the windiest month can reach 1000 W (m coastline)$^{-1}$.

(ii) IFREMER mixed layer depths (de Boyer Montégut et al. 2004), and (iii) global bathymetry (Smith and Sandwell 1997). The total wind work is 0.31 TW (Fig. 11a), which is comparable to other global models (Simmons and Alford 2012; Alford et al. 2016). Wind work is strongest [i.e., $\mathcal{O}(1)$ mW m^{-2}] along the storm tracks between 30° and 60° latitude, and generally an order of magnitude weaker at lower latitudes. However, individual tropical cyclones enhance wind work so that their tracks are visible in the 2-yr mean. Ten percent of wind work, that is, 0.03 TW, occurs within the coastal boundary zone defined by D and is, therefore, radiated from the coast as barotropic near-inertial waves.

Individual estimates of F_0 were computed from (32) using H and wind stress taken at the offshore limit of 989 continental slopes that are approximately 100 km apart (see Kelly et al. 2013). The 2-yr mean of F_0 reaches $\mathcal{O}(100)$ W (m coastline)$^{-1}$ on western boundaries and at high latitudes, but is $\mathcal{O}(10)$ W (m coastline)$^{-1}$ elsewhere (Fig. 11b). The global integral of F_0, using 100-km spacing, is 0.004 TW, about 10 times less than the estimate based on D. However, the estimate using F_0 omits generation in several coastal seas and uses a global coastline of 98 900 km, which is substantially less than the 356 000 km reported by the Central Intelligence Agency (2018). While F_0 is useful for examining geographic variability, its global integral is dubious.

Storms greatly enhance instantaneous energy fluxes because F_0 depends on wind speed to the fourth power (the square of wind stress). At each continental slope, the windiest month was identified from the maximum wind stress variance over a 30-day moving window.

Energy fluxes averaged over the windiest month are an order of magnitude greater than the 2-yr averages, for example, F_0 nearly reaches 1000 W (m coastline)$^{-1}$ in some locations, such as the east coast of North America (Fig. 11c).

Before moving on, it is worth reiterating that the exact fate of the radiated barotropic energy flux F_0 is unclear. The numerical simulation in section 5 indicated that near-inertial barotropic waves can generate internal waves at the shelfbreak, but the process was quite weak [$\mathcal{O}(10)$ W (m coastline)$^{-1}$; Fig. 10c] even after a major storm (Ernesto), suggesting that these waves may propagate long distances before dissipating. Basin-scale models are needed to determine whether coastally generated near-inertial barotropic waves primarily dissipate through bottom drag in shallow seas or topographic scattering in the deep ocean.

7. Summary and discussion

The results here detail how wind generates near-inertial internal waves along coastlines. These results are consistent with previous findings (e.g., Pettigrew 1980; Millot and Crépon 1981; Csanady 1982; Kundu et al. 1983; Baines 1986; Shearman 2005), but emphasize some new points:

- Wind-driven coastal flows can be separated into forced and wave motions, simplifying estimates of wind work and wave radiation.
- Wave radiation is a continuous process driven by broadband wind forcing, rather than isolated adjustments to wind impulses. Mixed layer velocities resonate at f, but waves can and do radiate at all frequencies, leading to highly intermittent flows. Bursts of wind may enhance or suppress existing currents depending on their phase.
- Locations without a vertical-wall coastline only generate an offshore propagating barotropic wave, which then scatters over topography as it propagates offshore. The typical expression for topographic generation (27) quantifies this scattering, but decomposing the barotropic flow into forced and wave components is nontrivial. Topographic scattering by coastally generated barotropic waves is a potential source of upward propagating near-inertial energy, which has been observed in the deep ocean (Alford 2010).
- Offshore near-inertial energy fluxes are typically less than 100 W (m coastline)$^{-1}$. However, energy flux depends on wind speed to the fourth power (the square of wind stress), so that a few major storms (e.g., tropical cyclones) can produce short periods of extreme energy fluxes that dominate long-term averages. Globally, we estimate that CNIWs radiate 0.03 TW of barotropic energy flux (i.e., 10% of wind work) to the deep ocean. The fate of this energy is completely unknown, although it is available to generate near-inertial internal waves through topographic scattering.

The application of this theory to the New Jersey shelfbreak is somewhat disappointing because it does not accurately predict observed near-inertial mixed layer transport or mode-1 pressure. Further research is needed to precisely quantify how the theory is hampered by simplifying assumptions and input uncertainties (such as wind stress). It also remains unclear whether the SW06 observations themselves are ''contaminated'' by remotely generated near-inertial internal waves. Fortunately, some of these problems can be avoided by analyzing realistic regional simulations and observations of near-inertial motions in an enclosed basin without tides. At present, data from a 20-mooring array in Lake Superior are being analyzed to further assess the theory presented here (E. Green 2019, personal communication).

Acknowledgments. This work was supported by the National Science Foundation Grant OCE-1635560 and Office of Naval Research Grant N00014-181-2800 (NISKINE). I am grateful to Jay Austin, Drew Lucas, Jonathan Nash, and Erica Green for numerous insightful conversations. Jonathan Nash kindly furnished the SW06 mooring data. Two anonymous reviewers provided insightful comments.

REFERENCES

Alford, M. H., 2001: Internal swell generation: The spatial distribution of energy flux from the wind to mixed layer near-inertial motions. *J. Phys. Oceanogr.*, **31**, 2359–2368, https://doi.org/10.1175/1520-0485(2001)031<2359:ISGTSD>2.0.CO;2.

——, 2003: Improved global maps and 54-year history of wind-work on ocean inertial motions. *Geophys. Res. Lett.*, **30**, 1424, https://doi.org/10.1029/2002GL016614.

——, 2010: Sustained, full-water-column observations of internal waves and mixing near Mendocino Escarpment. *J. Phys. Oceanogr.*, **40**, 2643–2660, https://doi.org/10.1175/2010JPO4502.1.

——, and M. Whitmont, 2007: Seasonal and spatial variability of near-inertial kinetic energy from historical moored velocity records. *J. Phys. Oceanogr.*, **37**, 2022–2037, https://doi.org/10.1175/JPO3106.1.

——, J. A. MacKinnon, H. L. Simmons, and J. D. Nash, 2016: Near-inertial internal gravity waves in the ocean. *Annu. Rev. Mar. Sci.*, **8**, 95–123, https://doi.org/10.1146/annurev-marine-010814-015746.

Austin, J. A., 2013: Observations of near-inertial energy in Lake Superior. *Limnol. Oceanogr.*, **58**, 715–728, https://doi.org/10.4319/lo.2013.58.2.0715.

Baines, P. G., 1986: Internal tides, internal waves, and near-inertial motions. *Baroclinic Processes on Continental Shelves*, C. N. K. Mooers, Ed., Coastal and Estuarine Sciences, Vol. 3, Amer. Geophys. Union, 19–31.

Brink, K., 1991: Coastal-trapped waves and wind-driven currents over the continental shelf. *Annu. Rev. Fluid Mech.*, **23**, 389–412, https://doi.org/10.1146/annurev.fl.23.010191.002133.

Cahn, A., 1945: An investigation of the free oscillations of a simple current system. *J. Meteor.*, **2**, 113–119, https://doi.org/10.1175/1520-0469(1945)002<0113:AIOTFO>2.0.CO;2.

Carwright, D. E., and R. D. Ray, 1991: Energetics of global ocean tides from Geosat altimetry. *J. Geophys. Res.*, **96**, 16 897–16 912, https://doi.org/10.1029/91JC01059.

Central Intelligence Agency, 2018: World Factbook. Central Intelligence Agency, https://www.cia.gov/library/publications/the-world-factbook/.

Chant, R. J., 2001: Evolution of near-inertial waves during an upwelling event on the New Jersey inner shelf. *J. Phys. Oceanogr.*, **31**, 746–764, https://doi.org/10.1175/1520-0485(2001)031<0746:EONIWD>2.0.CO;2.

Choi, J., C. D. Troy, T.-C. Hsieh, N. Hawley, and M. J. McCormick, 2012: A year of internal Poincaré waves in southern Lake Michigan. *J. Geophys. Res.*, **117**, C07014, https://doi.org/10.1029/2012JC007984.

Csanady, G. T., 1982: *Circulation in the Coastal Ocean*. Springer, 279 pp.

D'Asaro, E. A., 1985: The energy flux from the wind to near-inertial motions in the surface mixed layer. *J. Phys. Oceanogr.*, **15**, 1043–1059, https://doi.org/10.1175/1520-0485(1985)015<1043:TEFFTW>2.0.CO;2.

——, 1989: The decay of wind-forced mixed layer inertial oscillations due to the β effect. *J. Geophys. Res.*, **94**, 2045–2056, https://doi.org/10.1029/JC094iC02p02045.

——, C. C. Eriksen, M. D. Levine, P. Niler, C. A. Paulson, and P. Van Meurs, 1995: Upper-ocean inertial currents forced by a strong storm. Part I: Data and comparisons with linear theory. *J. Phys. Oceanogr.*, **25**, 2909–2936, https://doi.org/10.1175/1520-0485(1995)025<2909:UOICFB>2.0.CO;2.

de Boyer Montégut, C., G. Madec, A. S. Fischer, A. Lazar, and D. Iudicone, 2004: Mixed layer depth over the global ocean: An examination of profile data and a profile-based climatology. *J. Geophys. Res.*, **109**, C12003, https://doi.org/10.1029/2004JC002378.

Federiuk, J., and J. S. Allen, 1996: Model studies of near-inertial waves in flow over the Oregon continental shelf. *J. Phys. Oceanogr.*, **26**, 2053–2075, https://doi.org/10.1175/1520-0485(1996)026<2053:MSONIW>2.0.CO;2.

Garrett, C., and W. Munk, 1971: The age of the tide and the "Q" of the oceans. *Deep-Sea Res. Oceanogr. Abstr.*, **18**, 493–503, https://doi.org/10.1016/0011-7471(71)90073-8.

Gill, A. E., 1984: On the behavior of internal waves in the wakes of storms. *J. Phys. Oceanogr.*, **14**, 1129–1151, https://doi.org/10.1175/1520-0485(1984)014<1129:OTBOIW>2.0.CO;2.

Hall, R. A., J. N. Huthnance, and R. G. Williams, 2013: Internal wave reflection on shelf slopes with depth-varying stratification. *J. Phys. Oceanogr.*, **43**, 248–258, https://doi.org/10.1175/JPO-D-11-0192.1.

Hopkins, J. E., G. R. Stephenson, J. A. M. Green, M. E. Inall, and M. R. Palmer, 2014: Storms modify baroclinic energy fluxes in a seasonally stratified shelf sea: Inertial-tidal interaction. *J. Geophys. Res. Oceans*, **119**, 6863–6883, https://doi.org/10.1002/2014JC010011.

Jayne, S. R., and L. C. St. Laurent, 2001: Parameterizing tidal dissipation over rough topography. *Geophys. Res. Lett.*, **28**, 811–814, https://doi.org/10.1029/2000GL012044.

Jiang, J., Y. Lu, and W. Perrie, 2005: Estimating the energy flux from the wind to ocean inertial motions: The sensitivity to surface wind fields. *Geophys. Res. Lett.*, **32**, L15610, https://doi.org/10.1029/2005GL023289.

Jing, Z., L. Wu, and X. Ma, 2017: Energy exchange between the mesoscale oceanic eddies and wind-forced near-inertial oscillations. *J. Phys. Oceanogr.*, **47**, 721–733, https://doi.org/10.1175/JPO-D-16-0214.1.

Johnston, T. M. S., D. L. Rudnick, and S. M. Kelly, 2015: Standing internal tides in the Tasman Sea observed by gliders. *J. Phys. Oceanogr.*, **45**, 2715–2737, https://doi.org/10.1175/JPO-D-15-0038.1.

Kelly, S. M., 2016: The vertical mode decomposition of surface and internal tides in the presence of a free surface and arbitrary topography. *J. Phys. Oceanogr.*, **46**, 3777–3788, https://doi.org/10.1175/JPO-D-16-0131.1.

——, and P. F. J. Lermusiaux, 2016: Internal-tide interactions with the Gulf Stream and Middle Atlantic Bight shelfbreak front. *J. Geophys. Res. Oceans*, **121**, 6271–6294, https://doi.org/10.1002/2016JC011639.

——, N. L. Jones, J. D. Nash, and A. F. Waterhouse, 2013: The geography of semidiurnal mode-1 internal-tide energy loss. *Geophys. Res. Lett.*, **40**, 4689–4693, https://doi.org/10.1002/grl.50872.

——, P. F. J. Lermusiaux, T. F. Duda, and P. J. Haley Jr., 2016: A coupled-mode shallow-water model for tidal analysis: Internal tide reflection and refraction by the Gulf Stream. *J. Phys. Oceanogr.*, **46**, 3661–3679, https://doi.org/10.1175/JPO-D-16-0018.1.

Kundu, P. K., 1984: Generation of coastal inertial oscillations by time-varying wind. *J. Phys. Oceanogr.*, **14**, 1901–1913, https://doi.org/10.1175/1520-0485(1984)014<1901:GOCIOB>2.0.CO;2.

——, S.-Y. Chao, and J. P. McCreary, 1983: Transient coastal currents and inertio-gravity waves. *Deep-Sea Res.*, **30**, 1059–1082, https://doi.org/10.1016/0198-0149(83)90061-4.

Llewellyn Smith, S. G., and W. R. Young, 2002: Conversion of the barotropic tide. *J. Phys. Oceanogr.*, **32**, 1554–1566, https://doi.org/10.1175/1520-0485(2002)032<1554:COTBT>2.0.CO;2.

Mandelbrot, B., 1967: How long is the coast of Britain? Statistical self-similarity and fractional dimension. *Science*, **156**, 636–638, https://doi.org/10.1126/science.156.3775.636.

Marshall, J., A. Adcroft, C. Hill, L. Perelman, and C. Heisey, 1997: A finite-volume, incompressible Navier-Stokes model for studies of the ocean on parallel computers. *J. Geophys. Res.*, **102**, 5753–5766, https://doi.org/10.1029/96JC02775.

Millot, C., and M. Crépon, 1981: Inertial oscillations on the continental shelf of the Gulf of Lions—Observations and theory. *J. Phys. Oceanogr.*, **11**, 639–657, https://doi.org/10.1175/1520-0485(1981)011<0639:IOOTCS>2.0.CO;2.

Moehlis, J., and S. G. Llewellyn Smith, 2001: Radiation of mixed layer near-inertial oscillations into the ocean interior. *J. Phys. Oceanogr.*, **31**, 1550–1560, https://doi.org/10.1175/1520-0485(2001)031<1550:ROMLNI>2.0.CO;2.

Morse, P. M., 1948: *Vibration and Sound*. 2nd ed., McGraw-Hill, 468 pp.

Nash, J. D., S. M. Kelly, E. L. Shroyer, J. N. Moum, and T. F. Duda, 2012a: The unpredictable nature of internal tides on continental shelves. *J. Phys. Oceanogr.*, **42**, 1981–2000, https://doi.org/10.1175/JPO-D-12-028.1.

——, E. Shroyer, S. M. Kelly, M. Inall, T. Duda, M. Levine, N. Jones, and R. Musgrave, 2012b: Are any coastal internal tides predictable? *Oceanography*, **25**, 80–95, https://doi.org/10.5670/oceanog.2012.44.

Pettigrew, N. R., 1980: The dynamics and kinematics of the coastal boundary layer off Long Island. Ph.D. thesis, Massachusetts Institute of Technology, 262 pp., https://doi.org/10.1575/1912/3727.

Plueddemann, A. J., and J. T. Farrar, 2006: Observations and models of the energy flux from the wind to mixed-layer inertial

currents. *Deep-Sea Res. II*, **53**, 5–30, https://doi.org/10.1016/J.DSR2.2005.10.017.

Pollard, R. T., 1970: On the generation by winds of inertial waves in the ocean. *Deep-Sea Res. Oceanogr. Abstr.*, **17**, 795–812, https://doi.org/10.1016/0011-7471(70)90042-2.

——, and R. C. Millard, 1970: Comparison between observed and simulated wind-generated inertial oscillations. *Deep-Sea Res. Oceanogr. Abstr.*, **17**, 813–821, https://doi.org/10.1016/0011-7471(70)90043-4.

Price, J. F., 1983: Internal wave wake of a moving storm. Part I: Scales, energy budget, and observations. *J. Phys. Oceanogr.*, **13**, 949–965, https://doi.org/10.1175/1520-0485(1983)013<0949:IWWOAM>2.0.CO;2.

Shearman, R. K., 2005: Observations of near-inertial current variability on the New England Shelf. *J. Geophys. Res.*, **110**, C02012, https://doi.org/10.1029/2004JC002341.

Shroyer, E. L., J. N. Moum, and J. D. Nash, 2011: Nonlinear internal waves over New Jersey's continental shelf. *J. Geophys. Res.*, **116**, C03022, https://doi.org/10.1029/2010JC006332.

Simmons, H. L., and M. H. Alford, 2012: Simulating the long-range swell of internal waves generated by ocean storms. *Oceanography*, **25**, 30–41, https://doi.org/10.5670/oceanog.2012.39.

Smith, W. H. F., and D. T. Sandwell, 1997: Global sea floor topography from satellite altimetry and ship depth soundings. *Science*, **277**, 1956–1962, https://doi.org/10.1126/science.277.5334.1956.

Tang, D., and Coauthors, 2007: Shallow Water '06: A joint acoustic propagation/nonlinear internal wave physics experiment. *Oceanography*, **20**, 156–167, https://doi.org/10.5670/oceanog.2007.16.

Watanabe, M., and T. Hibiya, 2002: Global estimates of the wind-induced energy flux to inertial motions in the surface mixed layer. *Geophys. Res. Lett.*, **29**, 1239, https://doi.org/10.1029/2001GL014422.

Waterhouse, A. F., and Coauthors, 2018: Observations of the Tasman Sea internal tide beam. *J. Phys. Oceanogr.*, **48**, 1283–1297, https://doi.org/10.1175/JPO-D-17-0116.1.

Weller, R. A., 1982: The relation of near-inertial motions observed in the mixed layer during the JASIN (1978) experiment to the local wind stress and to the quasi-geostrophic flow field. *J. Phys. Oceanogr.*, **12**, 1122–1136, https://doi.org/10.1175/1520-0485(1982)012<1122:TRONIM>2.0.CO;2.

Wunsch, C., 2015: *Modern Observational Physical Oceanography: Understanding the Global Ocean*. Princeton University Press, 512 pp.

Young, W. R., and M. Ben Jelloul, 1997: Propagation of near inertial oscillations through a geostrophic flow. *J. Mar. Res.*, **55**, 735–766, https://doi.org/10.1357/0022240973224283.

Zhang, Y. G., and T. F. Duda, 2013: Intrinsic nonlinearity and spectral structure of internal tides at an idealized Mid-Atlantic Bight shelf break. *J. Phys. Oceanogr.*, **43**, 2641–2660, https://doi.org/10.1175/JPO-D-12-0239.1.